Next Materials 12 (2026) 102204

Contents lists available at ScienceDirect

Next Materials

journal homepage: www.sciencedirect.com/journal/next-materials

Research Article

Exploring the use of an auxetic metamaterial layer as external reinforcement for masonry columns

Luigi Salvatore Rainone [a], Luis C.M. da Silva [b], Giuseppina Uva [a], Siro Casolo [b,*]

[a] DICATECh Department, Politecnico di Bari, Bari, Italy
[b] ABC Department, Politecnico di Milano, Milano, Italy

ARTICLE INFO

Keywords:
Masonry
Column
Retrofitting
Reinforcement Layer
Auxetic
Metamaterial

ABSTRACT

The present study investigates the effectiveness of an externally bonded layer of auxetic metamaterial as reinforcement for square-section masonry columns by means of numerical analyses. Metamaterials characterized by engineered microstructures and tunable macroscopic properties offer the potential for optimizing the mechanical compatibility with the specific characteristics of the masonry substrate. In addition, their negative Poisson's ratio allows the compressed layer to laterally confine the masonry with a pressure that is proportional to the vertical loading. The proposed strengthening concept is evaluated with reference to monotonic compression tests reported in the literature. Two three-dimensional finite element macro-models are developed, in which the masonry is represented using Concrete Damage Plasticity, while the reinforcement layer material is modeled as a homogeneous, isotropic, linearly elastic continuum. A comprehensive sensitivity analysis is subsequently carried out, treating the Young's modulus and Poisson's ratio of the auxetic layer as independent parameters. The results indicate that, although currently examined primarily from a theoretical standpoint, the proposed solution has the potential to constitute an effective innovation for the reinforcement of masonry columns, provided that the current technological limitations associated with the industrial production of auxetic materials can be overcome.

1. Introduction

The experimental investigation and numerical modelling of masonry structures represent central themes in the structural engineering research aimed at developing theoretical, numerical, and technological tools for the protection of existing built heritage [1–5]. In historical buildings, masonry columns constitute particularly vulnerable structural elements [6], which can be strengthened using various established technologies [7,8]. A commonly adopted approach involves the application of fiber-reinforced materials with bidirectional weaving, bonded to the surface via epoxy resins [9–11]. The installation procedure for these systems typically comprises: (1) application of a levelling mortar layer; (2) primer application; (3) deposition of a first resin layer (commonly termed "bonding"); (4) fabric placement; and (5) application of a second resin layer (termed "impregnation"). This reinforcement strategy seeks to induce a confinement effect through the higher stiffness of the overlay, while also partially supporting the vertical axial load.

The present example identifies some key limitations in the conventional reinforcement approach. Although the redistribution of axial load facilitated by the reinforcement layer enhances the overall column capacity, the compressive strains in the layer—which exhibits a positive Poisson's ratio greater than that of masonry—generate interface stresses that could led to an earlier onset of debonding phenomena. This issue can be effectively mitigated by employing an auxetic metamaterial layer, which yields substantial performance improvements [12].

Within the domain of masonry column retrofitting, this study elucidates the pivotal role of next-generation materials— particularly metamaterials—in surmounting the constraints of traditional reinforcement systems. The capacity to tailor macroscopic mechanical properties, such as Young's modulus and Poisson's ratio, via engineered microstructures [13–15], combined with industrial-scale 3D printing fabrication [16], enables optimized interaction between the masonry substrate and reinforcement, thereby addressing inherent limitations of conventional materials.

Auxetic metamaterials, characterized by a negative Poisson's ratio, challenge the conventional paradigms of deformation in structural materials by enabling lateral contraction under compression. This geometric effect has been increasingly recognized as a powerful mechanism to enhance confinement, delay damage localization, and promote high energy dissipation. Recent applications in cementitious composites,

* Corresponding author.
E-mail address: siro.casolo@polimi.it (S. Casolo).

https://doi.org/10.1016/j.nxmate.2026.102204
Received 12 March 2026; Received in revised form 26 April 2026; Accepted 4 May 2026
Available online 9 May 2026

where brittleness and limited post-peak capacity remain critical limitations, have shown that auxetic architectures offer an alternative route to performance enhancement relying on geometry and not only on material strength. Additive manufacturing of auxetic lattice reinforcements for cement-based materials has advanced considerably, generating a growing body of experimental evidence that demonstrates substantial improvements in ductility and energy absorption. Experimental studies on cementitious composites incorporating 3D-printed auxetic meshes have shown that the key parameters governing their mechanical response and failure mode are cell topology, orientation, and polymer compliance. In particular, highly deformable auxetic reinforcements have been shown to transform brittle flexural failure into stable, damage-tolerant mechanisms characterized by markedly increased energy absorption [17,18]. Similar advances have been reported in lightweight cementitious composites, whose inherently low stiffness enhances the effectiveness of auxetic confinement [19].

Despite these advances, existing studies are largely fragmented. Experimental investigations predominantly focus on specific structural configurations, whereas numerical studies often rely on complex constitutive formulations without establishing a transparent link between microstructural topology and macroscopic mechanical response. A unified, mechanistic framework capable of consistently explaining how auxetic geometry governs confinement, bond behavior, ductility, and energy dissipation in cementitious components is still lacking. Addressing this gap requires modeling strategies that do not merely enrich classical continua by a phenomenological approach but are capable to embed microstructural mechanics directly into the constitutive description, thereby enabling predictive and design-oriented insights for next-generation composites for civil engineering applications.

Along this research trajectory, some authors of the present work have recently investigated the microstructure analytical design through heuristic molecular approaches [20,21]. These analytical studies have demonstrated that a clear algebraic relationship can be established between the topology of periodic assemblies and their macroscopic elastic properties. A key result is that planar periodic structures based on orthogonal textures may exhibit a theoretically isotropic response with increasingly negative Poisson's ratio, at the sole expense of increased compliance. Fig. 1 illustrates this concept through a rigid body–spring model (RBSM). Owing to its compatibility with additive manufacturing, this microstructure enables the fabrication of material sheets with macroscopically isotropic behaviour [22]. A representative auxetic mockup configuration inspired by these studies is schematically shown in Fig. 2; for clarity, the cell dimensions are larger than those expected in practical engineering applications. Building on this framework, the present study explores the theoretical application of such auxetic materials – arranged in one or more planar layers – to masonry columns composed of low elastic modulus blocks. Although primarily subjected to in-plane membrane stresses, these layers are assembled to provide a confinement effect. Under compressive loading, consistent with the dominant stress state in masonry columns, the negative Poisson's ratio induces a lateral restraint that increases proportionally with the applied load, representing the distinctive feature of the proposed strengthening concept.

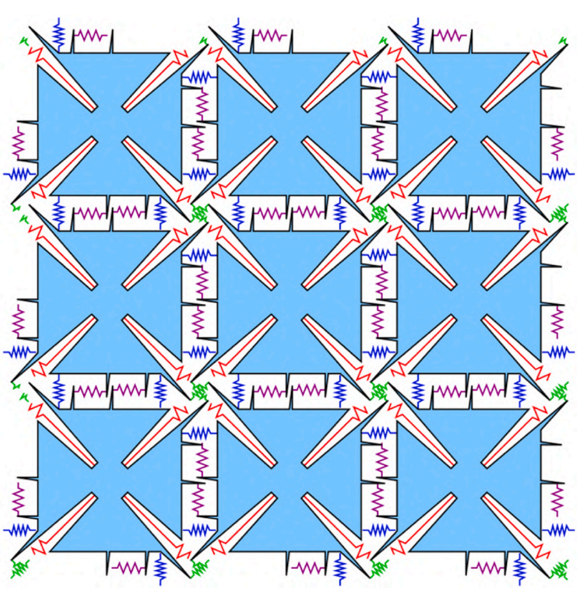

Fig. 1. Conceptual scheme based on the concept of Heuristic Molecules [20] forming an auxetic metamaterial layer.

To systematically investigate these phenomena and quantify the influence of the reinforcement layer's mechanical parameters on the column's structural response, a dedicated sensitivity analysis was conducted, with results presented across the subsequent nine sections. Section 2 reviews the most prevalent retrofitting techniques for masonry columns, identifying key opportunities for enhancement. Section 3 delineates the benchmark case study employed. Section 4 details the finite element (FE) numerical model [23] utilized for the sensitivity analyses. The outcomes of varying the Young's modulus and Poisson's ratio of the reinforcement layer are presented in Section 5 for modal analyses, Section 6 for quasi-static nonlinear push-down analyses, Section 7 for quasi-static nonlinear push-over analyses, and Section 8 for cyclic analyses. Section 9 offers concluding remarks, accompanied by proposals for future research directions.

2. Issues related to existing retrofitting techniques for masonry columns

The development of high-stiffness and high-strength fibers such as carbon, steel and glass has led to the creation of fabrics that can be adopted for the retrofitting of masonry structures. These are applied to the external surface of masonry columns, using epoxy resins as an adhesive, allowing for an increase in the stiffness, strength and ductility of the element.

The strategy of using reinforcement layers is often based on the concept of metal hooping that is widely used for the retrofitting of circular masonry columns (Fig. 3), proving to be a generally effective strategy [24]. In this case, the goal is to create a local confinement in the column, increasing the global strength of the structural element by virtue of the internal friction typically exhibited by masonry. However, the use of metal hoops is very effective mainly for structural elements with circular cross-section. Furthermore, during installation, the tensioning of the steel element should be limited to avoid the local damage to the structural element, reducing its load-bearing capacity. Clearly, the vertical load cannot be re-distributed to the steel elements, which merely contribute by giving a lateral containment.

The transposition of metal hooping principles to fiber-reinforced composites—bonded to the structural element's surface via resins to form a continuous layer—has overlooked critical theoretical implications. Unlike discontinuous metal hoops, the continuity of this layer alters system behavior significantly. Resin bonding enforces strain compatibility between the layer and the masonry core, such that uniaxial compressive strain in the column induces equivalent axial strain in the reinforcement. Differences in Young's modulus between the layer and masonry generate distinct axial deformability; however, resin-induced congruence provokes tangential stresses parallel to the column axis at their interface. These stresses must be accommodated by resin-masonry adhesion and the resin itself; failure leads to reinforcement detachment. More specifically, masonry and fiber-reinforced composites typically exhibit different positive Poisson's ratios, yielding differential transverse expansion under equivalent compressive strain. With the layer's Poisson's ratio exceeding that of masonry, the outer layer develops greater outward deformation than the core, inducing tensile forces at the four vertices—manifesting as interface shear stresses

Fig. 2. The mockups printed as single plane layer and as a 3-D box, based on the concept of auxetic Heuristic Molecule.

Fig. 3. Steel hoops on columns of the hypostyle hall in Maniace Castle in Syracuse, Italy.

and core tensile stresses (Fig. 4). Under vertical compression, any detachment exacerbates thin-layer instability, culminating in progressive layer failure and premature system collapse as loads intensify.

These considerations are consistent with the experimental results available in literature. Micelli et al. [25] report experimental tests conducted on full-scale columns reinforced with fiber-reinforced fabrics and show how the collapse of the retrofitted system is achieved with detachment and instability of the layer. A similar situation is found by Aiello et al. for brick and calcarenite block columns [26]; by Corradi et al. for octagonal columns reinforced with CFRP [27]; by Di Ludovico et al. for clay and tuff columns [28]; by Faella et al. for columns made of natural and artificial blocks [29]; by Krevaikas & Triantafillou for brick columns [30].

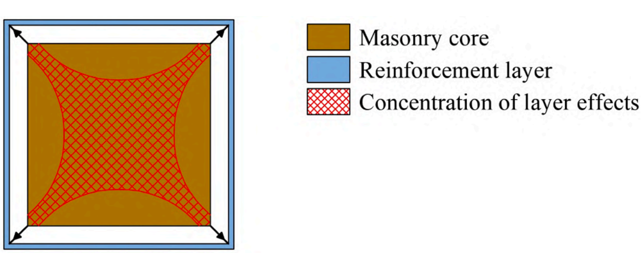

Fig. 4. Concentration of layer effects in the cross-section of the structural element due to the application of an external reinforcement layer with a Poisson's coefficient higher than that of masonry.

The analysis of this issue at the building scale reveals additional considerations for retrofitting interventions. Reinforcement layer materials exhibit macroscale stiffness exceeding that of the masonry composite, thereby altering the dynamic characteristics of the reinforced system relative to the original configuration. The increase of stiffness resulting after the retrofitting tends to reduce of the length of the natural periods of vibration that often corresponds to an increase in the reference seismic action (Fig. 5), while the change in modal shapes leads to a change in the distribution of forces induced by seismic action. Therefore, the use of retrofitting systems could alter the structural behavior and leads to unexpected collapse mechanisms. This, together with other factors of uncertainty, can lead to a significant decrease in the accuracy of structural safety assessment.

3. The case study: monotonic compression tests on a full-scale square masonry column

The experimental tests conducted by Micelli et al., 2014 [25] on unreinforced full-scale masonry columns with a square cross-section are here regarded as benchmark. The objective of these experiments was to evaluate the effectiveness of common technologies for the retrofitting of masonry columns. To this aim, two monotonic compression tests were also carried out on unreinforced columns. The essential traits of the case study are outlined in the following, also by adopting standard retrofitting techniques, while we address to the referred literature for further information about the tests and the results obtained.

The test columns had size of 0.40 m x 0.40 m x 2.10 m and were made of yellow limestone blocks with size of 0.13 m x 0.13 m x 0.40 m and with 5 mm thick lime and pozzolan mortar joints. The mortar was prepared using 310 kg/m^3 of binder, 1245 kg/m^3 of sand and 195 kg/m^3 of water to obtain an average resistance typical of pozzolanic mortar used in existing buildings. The average measured compressive strength of the blocks was 14.70 MPa. The average measured tensile strength of mortar was 1.60 MPa, while the average measured compressive strength was 5.50 MPa.

The full columns were then tested in a monotonic compression test according to the configuration in Fig. 6a. The lower base of each column was kept fixed while an axial load P was monotonically applied on the top according to a displacement-control procedure. The results obtained by the authors are shown in terms of damage maps in Fig. 6a and of stress-strain curves in Fig. 6c. A crushing failure mechanism was observed, with the propagation of vertical cracks both in blocks and in vertical mortar joints. Both tests exhibited a brittle failure with an average maximum load of 835 kN, corresponding to an average compressive stress of 5.22 MPa, and an axial strain about equal to

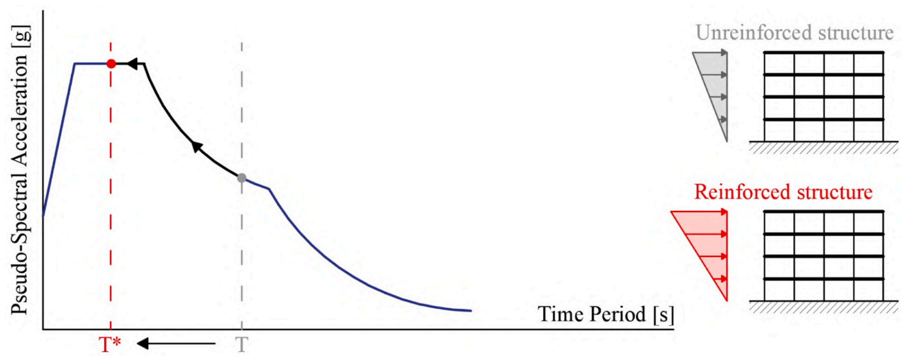

Fig. 5. Change in the reference Pseudo-Spectral Acceleration due to the retrofitting intervention: T is the reference period of the unreinforced structure; T* is the reference period for same structure after the intervention.

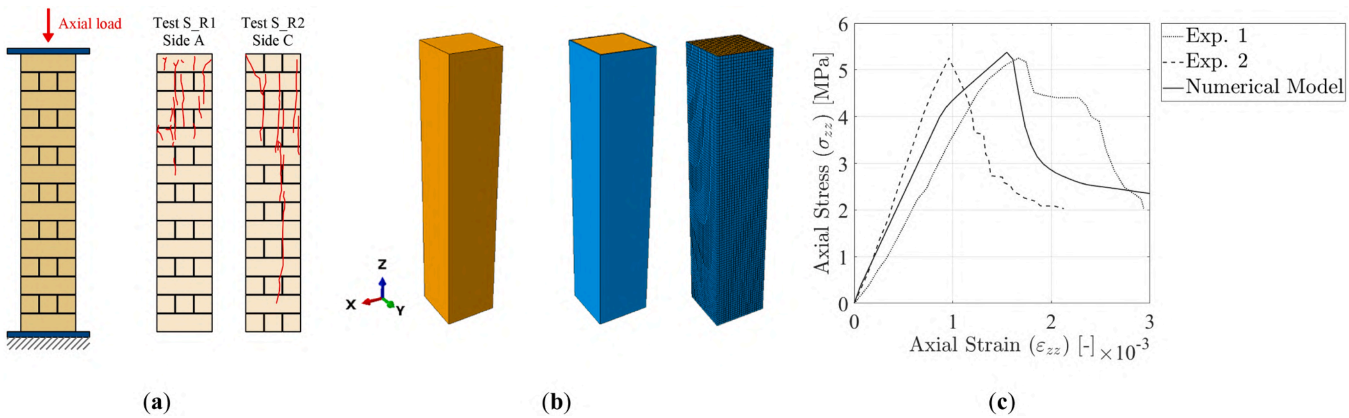

Fig. 6. Full-scale columns tests taken from literature: (a) experimental test setup and damage patterns observed; (b) numerical model implemented; (c) axial stress-strain relationships obtained experimentally and numerically.

0.15%.

4. Continuum three-dimensional FE macro-models implemented

This section presents the FE models implemented in Abaqus [23] for the numerical simulation of the experiments and for the evaluation of the theoretical effectiveness of the proposed metamaterials technology.

4.1. Geometrical modeling

For the purposes of this study, the full-scale masonry column described in Section 3 is modeled using finite elements within a designated reference triplet, wherein the z-axis aligns with the column's longitudinal axis, and the x- and y-axes lie within the cross-sectional plane. The numerical model excluding structural reinforcement layers is hereafter designated as the "unreinforced" configuration. To account for retrofitting interventions, a second three-dimensional model incorporates a 1 cm thick reinforcement layer applied to the column's outer surface. This layer is represented as a three-dimensional solid in perfect adherence to the masonry substrate, ensuring full contact and complete strain compatibility between the two components.

The mesh used for both models consists of C3D8 elements, i.e. general-purpose, fully integrated hexahedral elements (with $2 \times 2 \times 2$ integration points). The unreinforced model consists of 42,000 elements, while the reinforced model consists of 59,220 elements. Given the reduced thickness of the layer compared to the dimensions of the column and to prevent the mesh elements in the layer from being excessively distorted, in both cases an approximate size of 0.02 m is used for an average mesh element.

4.2. Mechanical modeling of the homogenized masonry continuum

This section describes the mechanical modelling strategy adopted for masonry. The behavior of the homogenized material assigned to the column is defined phenomenologically by assigning elastic and post-elastic characteristics that allow to reproduce the experimental results.

4.2.1. Constitutive Modeling of the Elastic Response

The masonry column is modelled as a homogeneous and isotropic continuum with the elastic parameters reported in Table 1. These parameters are derived from experimental data, setting the Young's modulus of the equivalent continuum equal to the stiffness measured by monotonic compression tests and adopting a typical value from the literature for Poisson's ratio, given the absence of experimental data in this regard. The density indicated in the literature for calcarenite blocks is assigned to the masonry continuum.

4.2.2. Modeling the post-elastic response through the concrete damage plasticity

The Concrete Damage Plasticity (hereafter CDP) is a material model

Table 1
Parameters adopted for modeling the elastic response and the mass properties of the masonry continuum.

Parameter	Nomenclature	Value
Young's Modulus	E_m	4500 MPa
Poisson's Coefficient	ν_m	0.15
Shear Modulus	G_m	1960 MPa
Mass Density	ρ_m	1600 kg/m^3

originally developed for modeling the behavior of concrete [31,32] and nowadays widely used in literature also for the micro- and macro-scale modeling of masonry structures [33–36]). The material model is available in the Abaqus material library without requiring the implementation of complex user-defined subroutines.

From a mechanical point of view, CDP is a continuum model in which the cracks' development is modeled by adopting a scalar isotropic damage with distinct damage parameters in tension and in compression, assuming that the main two failure mechanisms are tensile cracking and compressive crushing of the quasi-brittle material. It requires the preliminary assignment of a set of parameters that define the yield surface, the flow-rule and a viscous-plastic regularization, namely:

- ψ, dilatancy angle measured in the p-q plane, where p is the hydrostatic pressure and q the Von Mises equivalent stress.
- ϵ, eccentricity of the potential flow rule.
- σ_{b0}/σ_{c0}, ratio between the equi-biaxial compressive initial yielding stress and the uniaxial compressive initial yielding stress.
- $K_c = q_{TM}/q_{CM}$, parameter that modifies the Drucker-Prager yield function, being q_{TM} the second stress invariant on the tensile meridian and q_{CM} the second stress invariant on the compressive meridian.
- μ, viscosity parameter resulting from the use of a generalized Duvant-Lions regularization (Duvaut & Lions [37].

For the homogenized masonry material, given the absence of specific experimental data, the following values have been assumed: $\psi = 15°$; $\epsilon = 0.1$; $\sigma_{b0}/\sigma_{c0} = 1.16$; $K_c = 2/3$; $\mu = 0.0001$.

Subsequently, the material model requires the definition of the skeleton curves and of the damage variables both in tension and in compression. For the compression skeleton curve, a multi-linear discretization is adopted with an elastic branch $(O - E^-)$, by a hardening branch $(E^- - Y^-)$ and two softening branches $(Y^- - U^-, \quad U^- - S^-)$. The characteristic points of the compression skeleton curve are shown in Fig. 7a. The damage variable in compression (d_c) is given as a function of the inelastic strain (ε_c^{in}), defined as the total strain minus the elastic strain corresponding to the undamaged material. Table 2 shows, for each of the characteristic points, the value of the compressive stress σ_c, of the inelastic strain ε_c^{in} and the value of the damage variable d_c.

For the tension skeleton curve, a bilinear skeleton curve is adopted, with an elastic branch $(O - E^+)$, followed by a softening branch $(E^+ - S^+)$. The characteristic points of the compression skeleton curve are shown in Fig. 7b. The damage variable in tension (d_t) is given as a function of the cracking strain (ε_t^{ck}), defined as the total strain minus the elastic strain corresponding to the undamaged material. Table 2 shows, for each of the characteristic points, the value of the tensile stress σ_t, of the cracking strain ε_t^{ck} and the value of the damage variable d_t.

Table 2
CDP parameters adopted for modeling the compressive behavior of the homogenized masonry.

Points of the Skeleton Curve in Compression	Stress σ_c [MPa]	Inelastic Strain ε_c^{in} [-]	Damage in Compression d_c [-]
O	0	0	0
E^-	-3.938	0.000	0.000
Y^-	-5.250	0.000	0.000
U^-	-2.625	-1.313×10^{-3}	0.550
S^-	-2.100	-2.188×10^{-3}	0.750

Table 3
CDP parameters adopted for modeling the tensile behavior of the homogenized masonry.

Points of the Skeleton Curve in Tension	Stress σ_t [MPa]	Cracking Strain ε_t^{ck} [-]	Damage in Tension d_t [-]
O	0	0	0
E^+	0.394	0.000	0.000
S^+	0.000	0.088×10^{-3}	0.990

4.3. Mechanical modeling of the reinforcement layer and parameters for the sensitivity analysis

In the numerical model implemented in Abaqus, the external reinforcement layer is modelled as a homogeneous and isotropic continuum, with a linear-elastic behavior, making the collapse of the reinforced system attributable exclusively to the collapse of the masonry core. The Young's modulus and Poisson's ratio of the layer are treated as variables in a sensitivity analysis to investigate their influence on the response of the reinforced system. Moreover, the aim of this sensitivity analysis is also to assess the theoretical effectiveness of both existing retrofitting techniques and the proposed technology.

A perfect bond assumption is adopted as a simplifying hypothesis, in line with the comparative scope of the study. Since no experimental characterization of the layer–substrate interface was available for the benchmark case, no explicit contact model has been introduced. Furthermore, in the adopted configuration, the reinforcement mainly acts by providing lateral confinement to the column, so that interface effects are not explicitly considered. In fact, adhesion is ensured precisely by the fact that the lateral expansion of the masonry core, which is characterized by a positive Poisson's ratio, is restrained by the external auxetic layer, whose negative Poisson's ratio induces a confinement effect. Consequently, debonding is expected to be highly unlikely, especially when the adhesion mechanism is described through a Mohr–Coulomb-type model. In fact, conventional retrofitting solutions

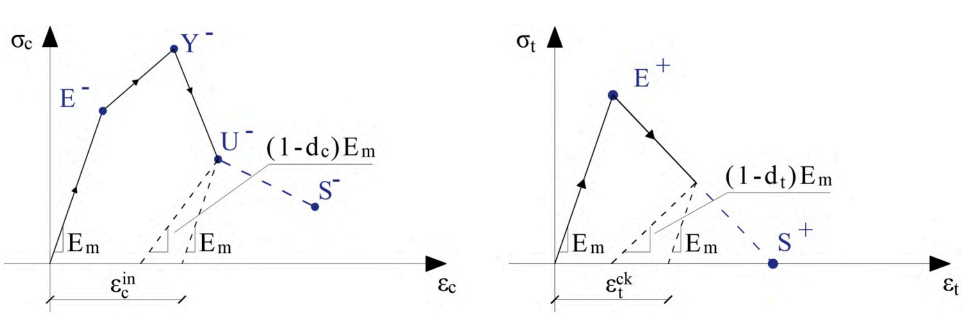

(a) (b)

Fig. 7. Skeleton curves defined for masonry material in: (a) compression; (b) tension.

typically rely on materials characterized by higher stiffness and higher Poisson's ratio compared to those commonly exhibited by masonry composites. In contrast, the use of a metamaterial with an engineered microstructure could allow the mechanical properties of the layer - specifically Young's modulus and Poisson's ratio - to be tailored a priori. This would enable improved mechanical compatibility between the retrofit layer and the existing structure, while potentially providing enhanced confinement of the structural cross-section. However, it is important to emphasize that Poisson's ratio significantly affects the structural compatibility through its influence on the shear modulus. In isotropic materials, according to Eq. (1), the relationship between Young's modulus (E) and shear modulus (G) depends directly on Poisson's ratio. Consequently, although a Poisson's ratio approaching the limit value of -1 is theoretically attainable, it corresponds to a very low E/G ratio under isotropic conditions. Such behavior is extremely challenging to achieve in practical engineering applications, particularly when compatibility with the masonry core material must be ensured.

$$\nu = \frac{E}{2G} - 1 \tag{1}$$

Therefore, in this study we perform a sensitivity analysis by varying the ratios E_l/E_m, hereafter referred to as the "stiffness-ratio", being the ratio between the Young's modulus of the layer (E_l) and the Young's modulus of masonry (E_m). On the other hand, the ratio ν_l/ν_m is hereafter referred to as the "deformability-ratio", which is the ratio between the Poisson's ratio of the layer (ν_l) and the Poisson's ratio of masonry (ν_m). A large stiffness ratio is representative of conventional reinforcement techniques, whereas the proposed meta-material technology is characterized by a stiffness ratio close to 1. Similarly, the condition $\nu_l > \nu_m$ reflects standard reinforcement strategies, while $\nu_l < 0$ corresponds to the proposed solution, which involves the use of auxetic meta-materials.

The sensitivity analysis is conducted by considering stiffness-ratio values E_l/E_m of 10, 5, and 1, and deformability-ratio values ν_l/ν_m equal to 2, 1, 0, -1, -2, and -3. Each combination of these parameters results in different corresponding values of the shear modulus of the layer (G_l). All the parameters adopted are shown in Table 4. Among the 21 cases analyzed, three are of greater engineering significance:

Case 1. $E_l/E_m = 10$ and $\nu_l = 0.30$. It represents a typical case of FRP with stiffness and transverse deformability greater than masonry.

Case 2. $E_l/E_m = 5$ and $\nu_l = -0.45$. It represents an improvement on standard technologies with better compatibility and a negative Poisson 's ratio for section confinement.

Case 3. $E_l/E_m = 1$ and $\nu_l = -0.45$. It represents a theoretical maximization of compatibility (difficult to achieve with current technologies) and a negative Poisson.

A comprehensive analysis of all the proposed cases is deemed necessary in order to achieve a thorough understanding of how the macro-structural behavior of the reinforced system depends on the mechanical properties of the layer.

Table 4
Values adopted for Young's Modulus and for Poisson's Ratio of the external reinforcement layer.

E_l/E_m	E_l [MPa]	ν_l/ν_m	ν_l [-]	G_l/G_m	G_l [MPa]
10	45,000	2	0.30	8.85	17,310
		1	0.15	10.00	19,570
		0	0.00	11.50	22,500
		-1	-0.15	13.53	26,470
		-2	-0.30	16.43	32,140
		-3	-0.45	20.91	40,910
5	22,500	2	0.30	4.42	8650
		1	0.15	5.00	9780
		0	0.00	5.75	11,250
		-1	-0.15	6.76	13,240
		-2	-0.30	8.21	16,070
		-3	-0.45	10.45	20,450
1	4500	2	0.30	0.88	1730
		1	0.15	1.00	1960
		0	0.00	1.15	2250
		-1	-0.15	1.35	2650
		-2	-0.30	1.64	3210
		-3	-0.45	2.09	4090

4.4. Validation of the proposed FE macro-model in reproducing the experiments results

With the aim of validating the numerical model implemented in Abaqus and described in Sections 4.1 and 4.2, the unreinforced configuration is subjected to a uniaxial compression test following the loading scheme illustrated in Fig. 5b. The base of the model is fully constrained such that, for every node P belonging to the mesh of the bottom cross section, is imposed $u_x(P) = u_y(P) = u_z(P) = 0$. Then, a monotonically increasing axial stress $\sigma_{zz}(t)$ is applied to the top surface in a displacement-control procedure. The results of the numerical analysis are presented in Fig. 6c.

The comparison with the experimental data shows that the model accurately reproduces: (i) the initial elastic stiffness observed in test S_{R2}; (ii) the progressive stiffness degradation occurring experimentally at stress levels of approximately 4 MPa; (iii) the peak compressive strength, equal to $f_c = 5.40$ MPa; and (iv) the pronounced post-peak softening up to a limit axial strain ε_{zz} of about 3‰. These results confirm that the adopted material parameters are appropriate for reliably simulating the experimental response.

5. Results of modal analysis

In this section, the results of the modal analyses are presented and discussed. In the first analysis step, a 30-tons lumped mass is placed on the top of the FE models of both structural configurations (i.e., the unreinforced and the reinforced column) to simulate the load acting on the column under realistic structural conditions (Fig. 8a). For the calculation of the lumped mass, the column is assumed to be located in a two-storey masonry building with cast-in place clay–cement floor slabs. Each floor slab has an overall thickness of 30 cm and consists of hollow clay blocks measuring $38 \times 25 \times 25$ cm^3, joists with a 12×25 cm^2 cross-section, and a 5 cm thick topping layer. Based on these characteristics, a floor load of 3.60 kN/m^2 is obtained. Assuming an influence area of 36 m^2 transferring load to each column and accounting for their self-weight, the resulting total applied load is 277.84 kN. This value is conservatively rounded to 300 kN, corresponding to approximately 30 tons. The mass is assumed to be in full contact with the column, and the corresponding solid elements are considered infinitely rigid. The base of each column is constrained by means of pinned supports. The results of the modal analysis are reported in Fig. 9 and discussed with reference to the first vibration mode (flexural, with oscillation along the x-axis) and the third vibration mode (axial, with oscillation along the z-axis). The second vibration mode, which is also flexural, exhibits modal characteristics identical to the first mode due to the double symmetry of the column cross-section.

The analysis of the results obtained for the flexural mode (Fig. 9a) shows that the natural vibration period of the reinforced column is strongly dependent on the Young's modulus of the layer, while it is only weakly influenced by its Poisson's ratio.

For a value of $E_l/E_m = 10$, a significant reduction in the natural vibration period is observed, decreasing from approximately 0.6 s to about 0.4 s. A reduction in the stiffness ratio leads to a smaller variation in the period of the first mode, thereby improving compatibility and, consequently, avoiding significant alterations of the reference seismic action for the structure within a broader engineering context. Similar considerations can be made on the axial vibration mode (Fig. 9b), for which a value of $E_l/E_m = 1$ also provides a high degree of layer–structure

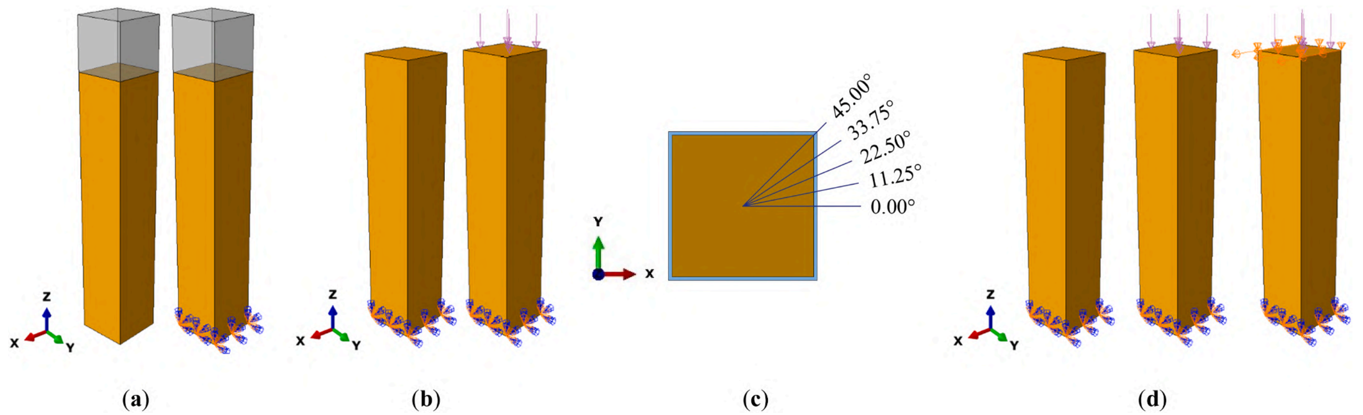

Fig. 8. Boundary conditions and steps followed for the numerical analysis of both reinforced and unreinforced models: (a) Modal analysis; (b) Non-linear monotonic compression analyses; (c) Directions in the X-Y plane adopted for push-over analyses; (d) Push-over analyses.

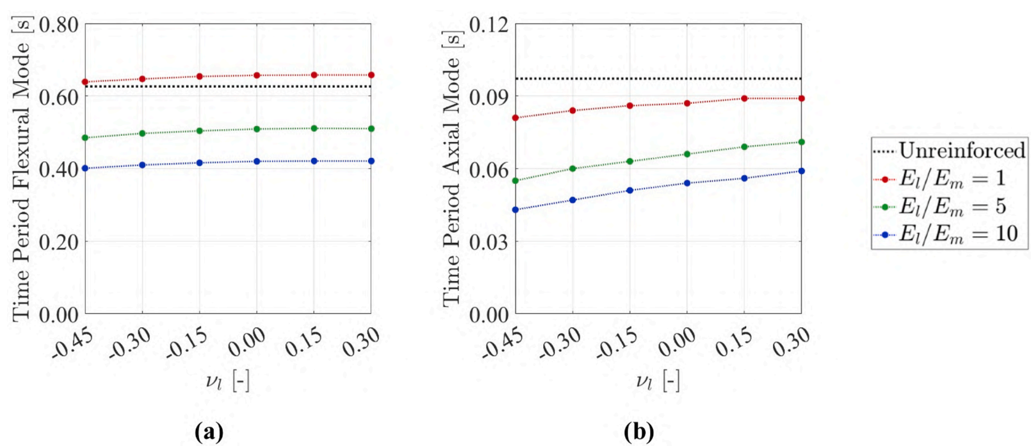

Fig. 9. Time period obtained for each reinforcement layer for: (a) flexural mode; (b) axial mode.

compatibility.

6. Non-linear monotonic analyses: compressive response

In this section, the results obtained from the push-down analyses are presented. In these analyses, both models are subjected to a monotonically increasing axial compressive load applied through a displacement-controlled procedure. The analysis is performed in two steps. In the first step, the base of the column is constrained (Fig. 8b). In the second step, an axial stress $\sigma_{zz}(t)$ is applied, monotonically increasing according to a displacement-controlled procedure. In order to reproduce the experimental results, the load is applied until a top displacement $u_z^{top} = -0.65$ cm is reached. The results obtained from the numerical simulations are analyzed in terms of the relationship between the axial stress $\sigma_{zz}(t)$ applied at the column top and the resulting axial strain $\varepsilon_{zz}(t)$.

The adoption of a reinforcement layer with $E_l/E_m = 10$ (Fig. 10a) consistently results in an increase in stiffness and strength. However, it is important to note that a reduction in the Poisson's ratio of the layer leads to both an increase in load-carrying capacity and a better post-

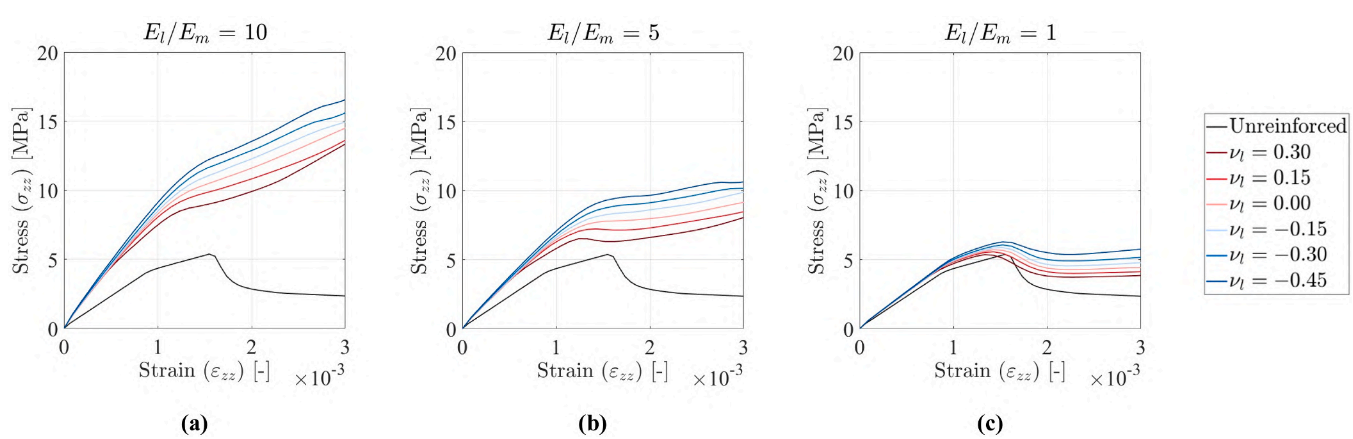

Fig. 10. Axial strain-stress relationships obtained from push-down analyses performed for each reinforcement layer: (a) $E_l/E_m = 10$; (b) $E_l/E_m = 5$; (c) $E_l/E_m = 1$.

elastic response. A ratio $E_l/E_m = 5$ (Fig. 10b) provides greater compatibility in terms of stiffness and, when combined with a negative Poisson's ratio, avoids the softening behavior observed in the experimental curve. Conversely, the adoption of a layer with $E_l/E_m = 1$ (Fig. 10c) results in a stiffness of the reinforced system comparable to that of the original system. In this case, a negative Poisson's ratio leads to an increase in strength and to a doubling of the load at ultimate strain, as a result of the sectional confinement effect.

By comparing the strength and stiffness obtained for the different stiffness-ratios and deformability-ratios of the reinforcement layer (Fig. 11), it emerges that the use of a negative Poisson's ratio consistently results in an improvement in strength for a given stiffness ratio. Furthermore, the possibility of predefining the macroscopic stiffness of the reinforcement layer through the design of its microstructure allows this parameter to be optimized in order to achieve a desired increase in strength while limiting the increase in stiffness. This can also be achieved while maintaining compatibility with the reference seismic action for the site where the intervention is implemented.

To highlight the stress-related challenges posed by conventional retrofitting techniques and demonstrate the remedial potential of an auxetic layer, the distribution of the stress component across the column's cross-section (at mid-height) is examined (Fig. 12).

The stress field reveals that a reinforcement layer with elevated stiffness ratio and a Poisson's ratio exceeding that of the masonry composite induces tensile stresses at the section edges and within the core, peaking at 0.40 MPa (Fig. 12a). These tensile stresses approach the limit tensile strength of masonry, predisposing the system toward tensile failure. The reduction of the stiffness ratio mitigates the tensile stress magnitude (Fig. 12b), yet fails to eliminate the issue entirely. Conversely, a high-stiffness auxetic layer with $\nu = -0.45$ generates compressive core stresses up to 1 MPa (Fig. 12c), a pattern replicated at unitary stiffness ratio (Fig. 12d). This compressive state fosters Coulomb-like frictional behavior, thereby enhancing the overall column capacity.

7. Non-linear monotonic analyses: shear response

In this section, the results obtained by subjecting both models to a shear force applied at the top of the column through a displacement-controlled procedure are presented. The analyses are performed by varying both the direction of the force and the precompression load. Considering the double geometric symmetry of the cross-section, five loading directions in the plane $\{O, \quad x, \quad y\}$ are considered, with inclination angle θ ranging from 0.0° to 45.0° (Fig. 8c). The analyses are carried out in three steps (Fig. 8d). In the first step, the base of the column is constrained. In the second, a precompression load σ_p varying between 0.00, 0.50, and 1.00 MPa is applied. In the third step, the top surface is constrained to keep constant the z-displacement recorded at the end of the second step. After, a lateral load $F_\theta(t) = \{F_x(t), \quad F_y(t)\}$ is applied to the top and monotonically increased according to a displacement-controlled procedure until $u_\theta^{top} = |u_x^{top}, \quad u_y^{top}| = 1.00$ cm is reached.

The results obtained by varying the Poisson's ratio of the reinforcement layer, the stiffness ratio, and the precompression load are analyzed in terms of stiffness and maximum load attained. Fig. 13 shows the variation of the first-cracking stiffness (evaluated at $u_\theta^{top} = 0.4$ mm) as a function of the loading direction and the applied precompression load. An increase in the stiffness-ratio consistently results in an increase in shear stiffness. The stiffness does not vary significantly with changes in the precompression load or the loading direction. A large negative Poisson's ratio amplifies the stiffness differences due to variations in the stiffness-ratio, as a consequence of the higher shear modulus G_l of the reinforcement layer. A high stiffness-ratio (Figs. 13a, 13b) promotes an anisotropic response of the column, both for a high and negative Poisson's ratio, and for high values of precompression load. Conversely, a layer with a lower stiffness ratio leads to a small variation, with the first-cracking stiffness largely independent of the applied precompression load (Fig. 13c).

Fig. 14 shows that an increase of the stiffness-ratio leads to a strength increase due to the higher fraction of total load carried by the reinforcement layer. Moreover, adopting a layer with reduced stiffness ($E_l/E_m = 5$) and a Poisson's ratio −0.45 provides benefits comparable to those of a standard layer ($E_l/E_m = 10$ and $\nu_l = 0.30$), while maintaining the stiffness of the reinforced system much closer to that of the unreinforced one. Furthermore, the ability to define a-priori the stiffness of the layer, together with its Poisson's ratio, allows the layer to be designed for achieving a target increase in structural strength. The variation of the pre-compression load does not significantly affect the shear capacity of the reinforced column. It should be noted, however, that this result depends on the value assigned to the dilatancy.

8. Results of non-linear cyclic analyses

In this section, the cyclic shear response of the column in the two configurations is investigated by applying a displacement along the x-direction varying according to the time history shown in Fig. 15. The analyses are carried out in two steps (Fig. 8d), analogous to those presented in Section 7 for the push-over analyses. In the first step, the base of the column is constrained using pinned supports. Subsequently, a displacement $u_x(t)$ is applied with $t \in [0.0, 10.0]$, while imposing that for all the points P on the top surface the conditions $u_z(P, t) = 0$ holds for every t.

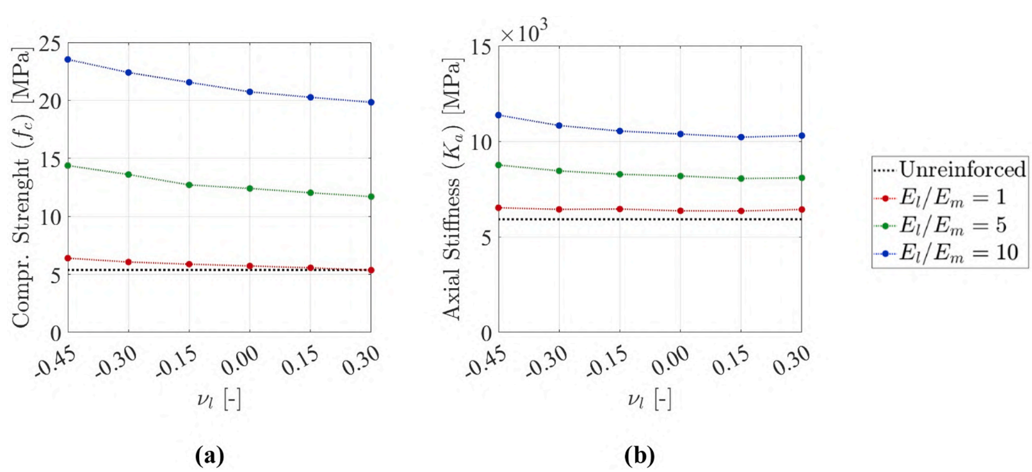

Fig. 11. Effects of the Poisson's Ratio of the layer and of the *stiffness-ratio* on the compressive response of the column: (a) compressive strength; (b) axial stiffness.

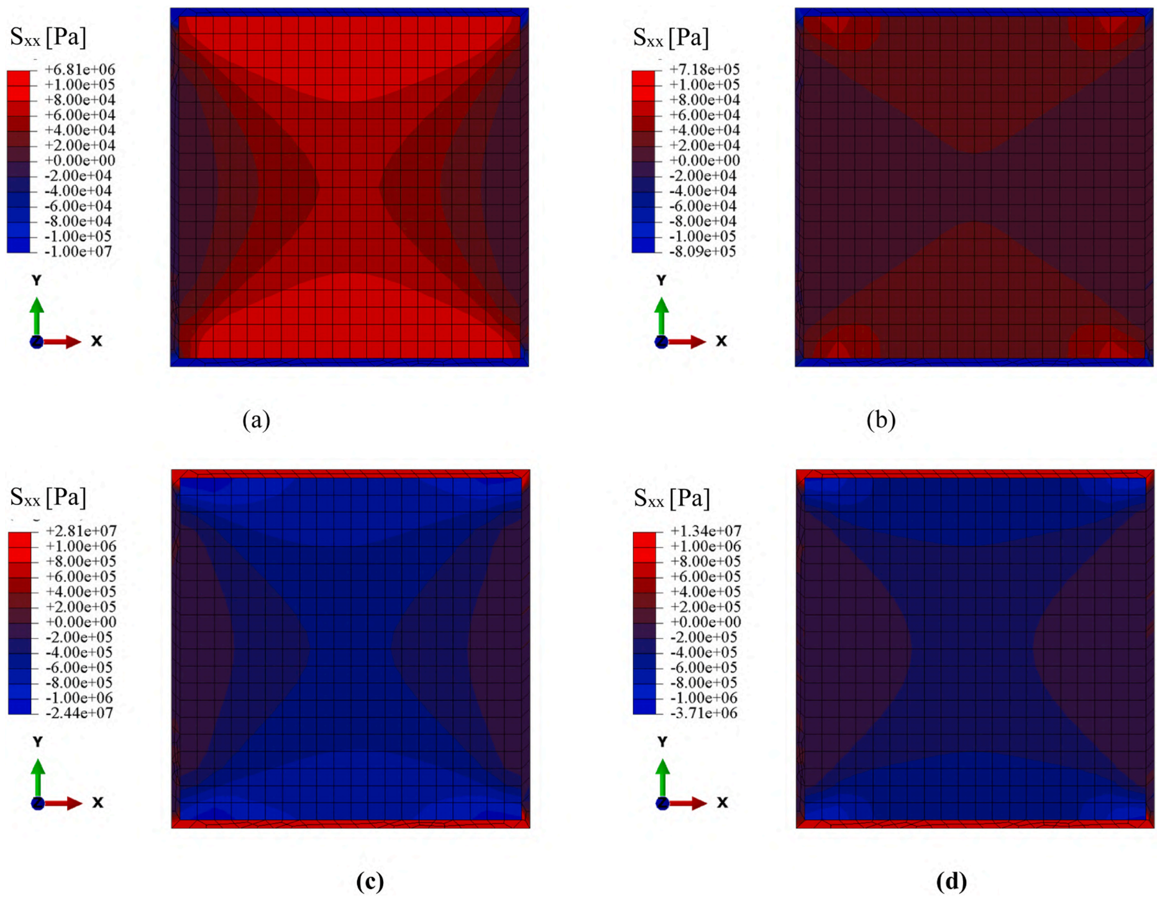

Fig. 12. Transversal stress component S_{xx} [Pa] induced by the axial load in the section corresponding to $z = 1.05$ m. Maps obtained for: (a) $E_l/E_m = 10$ and $\nu_l/\nu_m = 2$; (b) $E_l/E_m = 1$ and $\nu_l/\nu_m = 2$; (c) $E_l/E_m = 10$ and $\nu_l/\nu_m = -3$; (d) $E_l/E_m = 1$ and $\nu_l/\nu_m = -3$.

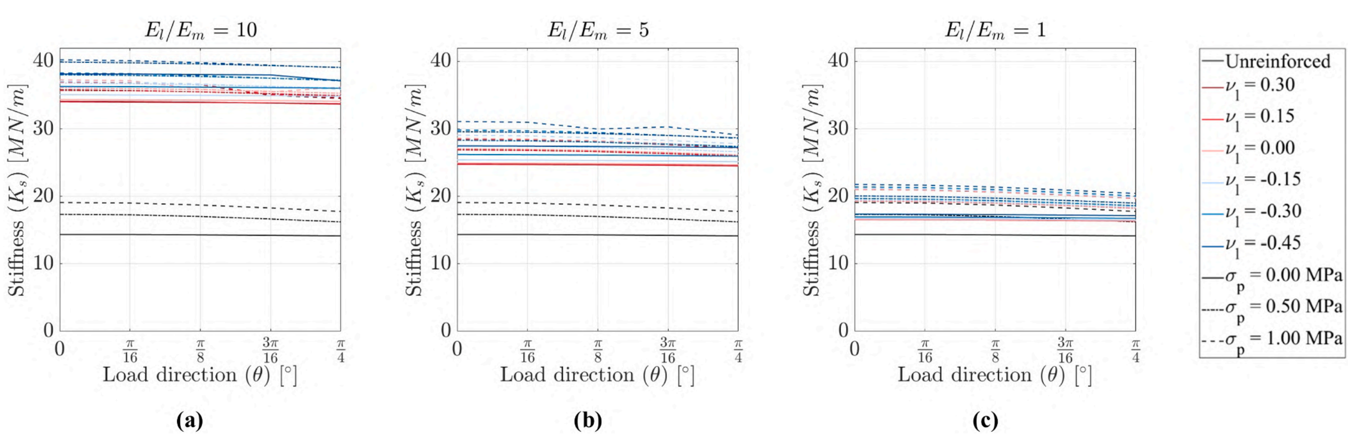

Fig. 13. Shear Stiffness obtained adopting different values of the stiffness-ratio and of precompression load: (a) $E_l/E_m = 10$; (b) $E_l/E_m = 5$; (c) $E_l/E_m = 1$.

The results obtained are analyzed in terms of force–displacement curves and energy balance, with the aim of assessing the macro-mechanical performance of the column and to investigate how the reinforcement layer influences the distribution and dissipation of energy of the system. The software Abaqus provides as output the energy components reported in Eq. 2. For clarity of presentation, these components are identified in this manuscript using the notation adopted by Abaqus [23]. Accordingly: ALLIE denotes the internal energy; ALLSE the elastic strain energy; ALLPD the inelastic dissipated energy; ALLCD the energy dissipated through viscoelasticity; ALLAE the artificial strain energy; ALLDMD the energy dissipated through damage; ALLDC the energy dissipated through distortion control; ALLFC the fluid cavity energy. In order to analyze the influence of the reinforcement layer on the energy balance and on the dissipation mechanisms of the system, the evolution of the energy components ALLSE, ALLPD, and ALLDMD is examined with respect to ALLIE.

$$ALLIE = ALLSE + ALLPD + ALLCD + \mathrm{ALLAE} + ALLDMD + ALLDC + ALLFC \quad (2)$$

The results obtained in terms of the force–displacement relationship (Fig. 16) are consistent with expectations: given the elasticity of the reinforcement layer, higher stiffness values lead to higher forces for the

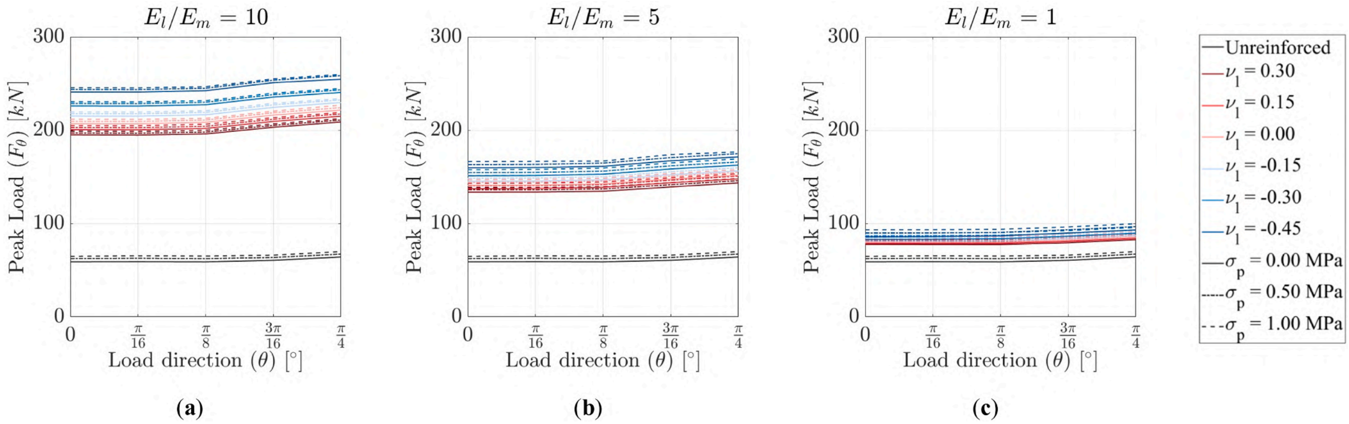

Fig. 14. Peak lateral load reached adopting different values of the *stiffness-ratio* and of precompression load: (a) $E_l/E_m = 10$; (b) $E_l/E_m = 5$; (c) $E_l/E_m = 1$.

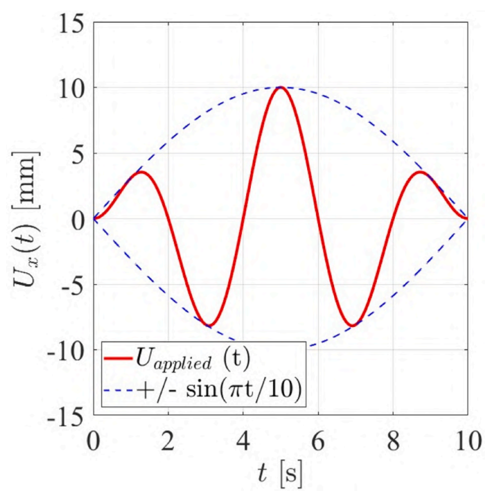

Fig. 15. Evolution of the applied displacement during the cyclic shear analysis.

same displacements. However, the analysis of the hysteretic curves shows that a standard reinforcement layer (with a positive Poisson's ratio) and $E_l/E_m = 10$ produces a significant increase in both the lateral stiffness and strength of the column. By keeping the stiffness ratio constant and reducing the Poisson's ratio, an additional increase in both stiffness and cyclic shear strength is observed. A lower stiffness ratio results in a smaller contribution of the layer to the overall column strength; nevertheless, adopting a Poisson's ratio of −0.45 still results in a strength increase compared to a layer with $\nu_l = 0.30$ (i.e., conventional reinforcement technologies). A unit stiffness ratio, although optimal for compatibility with the existing masonry, does not provide a strength increase large enough to justify its engineering application.

The analysis of the results in terms of elastic strain energy (Fig. 17) shows that, for each stiffness ratio, the use of a reinforcement made by a meta-material layer with negative Poisson's ratio increases the fraction of elastic energy stored in the system. With a unit stiffness ratio and a Poisson's ratio −0.45, the reinforced system initially behaves similarly to the unreinforced one. However, as the loading history progresses, the system response is predominantly elastic, and the auxetic layer promotes the storage of the applied load work predominantly as elastic strain energy.

The analysis of the time history of inelastic dissipated energy (ALLPD, Fig. 18) shows a behavior complementary to that observed for elastic strain energy. Standard reinforcement layers promote energy dissipation through plastic deformation, which facilitates masonry cracking induced by tensile stresses. In contrast, auxetic layers exhibit plastic dissipation significantly higher compared to the unreinforced model but lower than reinforcements having a positive Poisson's ratio.

The unreinforced system mainly stores the initial energy as elastic strain energy. Reinforcements with stiffness ratios of 10 or 5 accelerate the onset of plastic dissipation. A unitary stiffness ratio reproduces the original elastic storage tendency, thus representing the least invasive intervention.

In terms of damage-dissipated energy (ALLDMD, Fig. 19), it is observed that a high stiffness-ratio leads to a substantial independence from the Poisson's ratio of the reinforcement layer. As the stiffness ratio

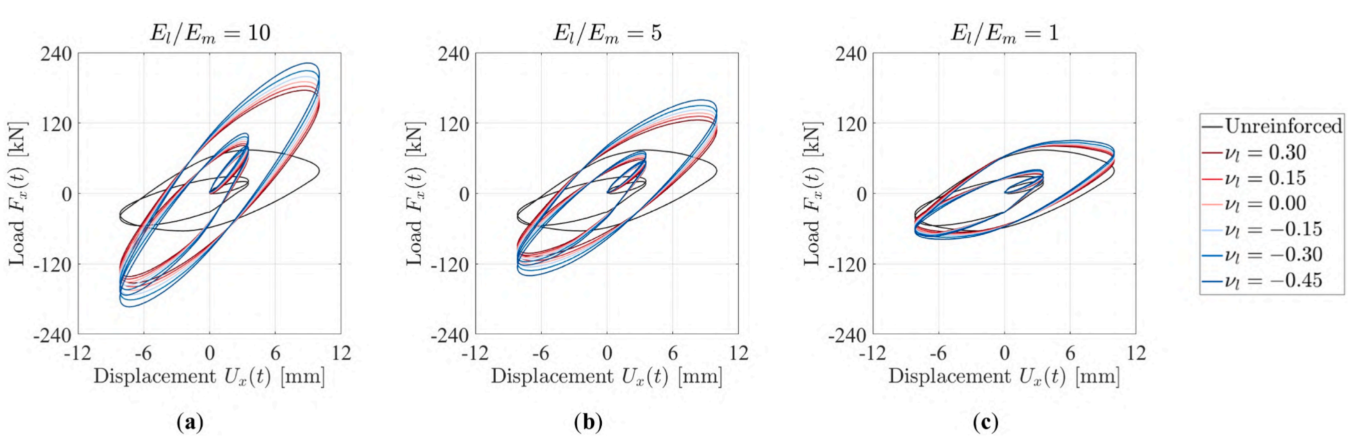

Fig. 16. Axial load-displacement relationships obtained from cyclic push-over analyses performed for each reinforcement layer: (a) $E_l/E_m = 10$; (b) $E_l/E_m = 5$; (c) $E_l/E_m = 1$.

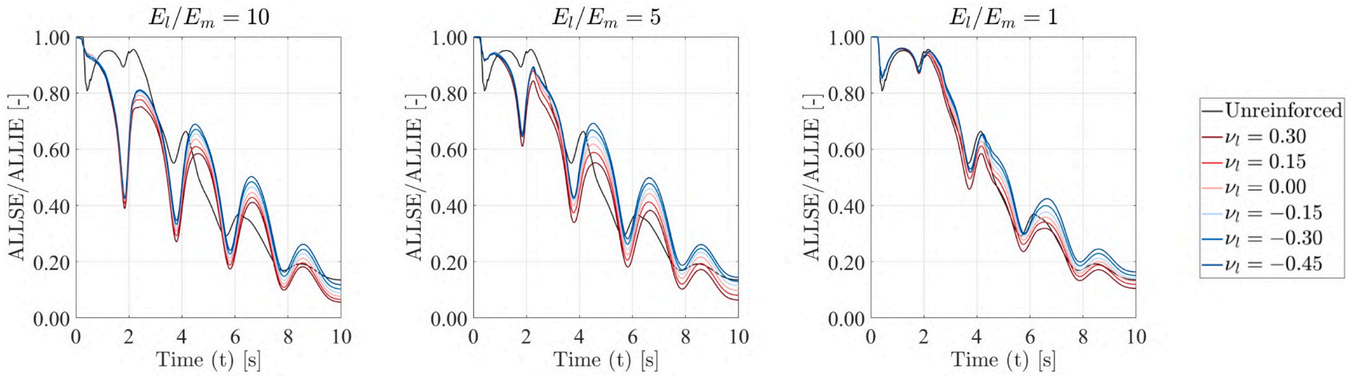

(a) **(b)** **(c)**

Fig. 17. Evolution of the Elastic Strain Energy over Internal Energy (ALLSE/ALLIE) during the cyclic push-over analyses performed for each reinforcement layer: (a) $E_l/E_m = 10$; (b) $E_l/E_m = 5$; (c) $E_l/E_m = 1$.

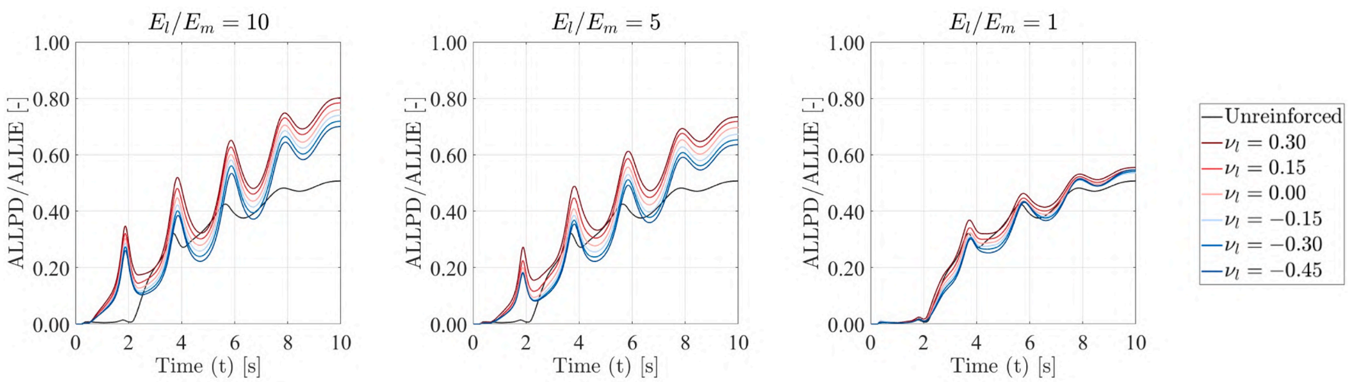

(a) **(b)** **(c)**

Fig. 18. Evolution of the Plastic Dissipated Energy over Internal Energy (ALLPD/ALLIE) during the cyclic push-over analyses performed for each reinforcement layer: (a) $E_l/E_m = 10$; (b) $E_l/E_m = 5$; (c) $E_l/E_m = 1$.

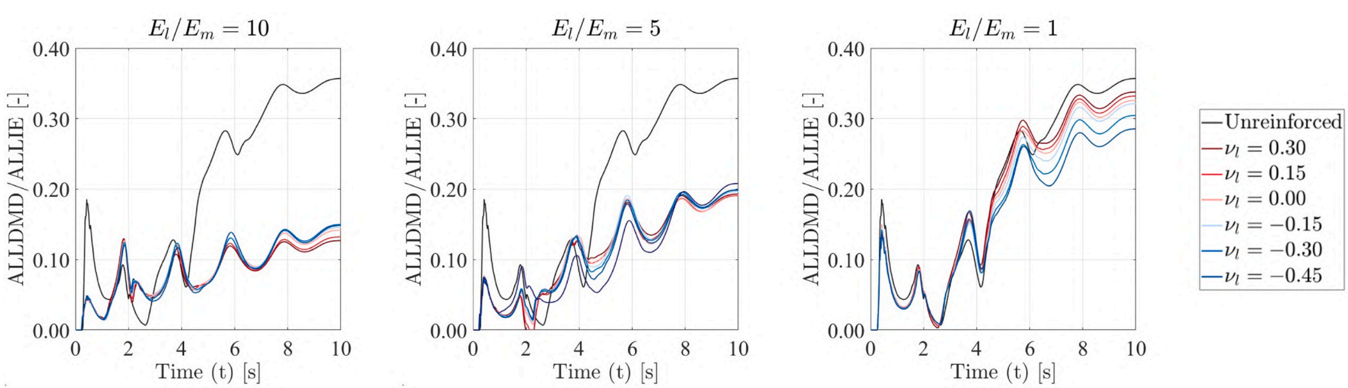

(a) **(b)** **(c)**

Fig. 19. Evolution of the Damage Dissipated Energy over Internal Energy (ALLDMD/ALLIE) during the cyclic push-over analyses performed for each reinforcement layer: (a) $E_l/E_m = 10$; (b) $E_l/E_m = 5$; (c) $E_l/E_m = 1$.

decreases, this trend is no longer observed. In the case of a unitary stiffness-ratio, while a standard retrofitting system is largely ineffective in limiting the energy dissipated through damage, a layer with a negative Poisson's ratio can reduce this damage-related energy dissipation.

9. Concluding remarks and future developments of the research

This pilot study evaluates the theoretical efficacy of a novel retrofitting technique for masonry columns, employing a homogeneous, isotropic auxetic meta-material layer. The reinforcing layer is a thin element primarily subjected to membrane stress states, i.e., stresses acting within its own plane. Accordingly, the assumed 2-D isotropy of the microstructure and the adoption of the corresponding macroscale shear modulus refer exclusively to the in-plane behavior of a relatively thin layer, which is the relevant response in the present application. No 3-D isotropy is assumed or required, particularly in the thickness direction, since out-of-plane contributions are not significant here. A comprehensive sensitivity analysis of the layer's Young's modulus and Poisson's ratio highlights the limitations of conventional technologies and underscores the advantages of the proposed approach. From a practical perspective, the proposed auxetic reinforcement may be conceived as a prefabricated or 3-D printed external layer, conceptually similar to FRP-based confinement systems used for masonry and concrete strengthening. However, since the present work is focused on the theoretical and numerical aspects, the feasibility investigation of real-scale applications remains beyond its scope and will require future dedicated experimental and technological validation.

The results concerning strength increase, confinement effects, and energy response should be interpreted as comparative numerical predictions, useful for highlighting trends and relative differences among the analyzed configurations, rather than as quantitative estimates of performance. We point out, once again, that the aim of this work is not to provide a complete experimental validation of the strengthened system, but rather to isolate and numerically analyze the effect of the layer while keeping other modeling assumptions unchanged. From this perspective, the validation of the unreinforced case provides the basis for model consistency, whereas the strengthened cases should be regarded as exploratory numerical extensions. Finally, we have not introduced a direct comparison with experimentally tested FRP-strengthened columns, since differences in geometry, materials, interface conditions, construction details, and loading protocols would make such a comparison not fully consistent with the adopted model.

The modal analysis reveals that standard reinforcement layers, characterized by macroscale stiffness exceeding that of the masonry column, substantially reduce vibration periods, thereby amplifying seismic demand. Metamaterials mitigate this effect through microstructure engineering, enabling a-priori stiffness calibration to match masonry properties. Push-down analyses demonstrate that stiff reinforcements with positive Poisson's ratios enhance load-bearing capacity but induce tensile stresses in the core and edges, potentially precipitating premature failure given masonry's low tensile strength. In contrast, auxetic layers with reduced stiffness and negative Poisson's ratios provide load-modulated confinement, engendering a hoop-stress effect that synergizes with masonry's frictional behaviour to increase resistance. Push-over analyses indicate that reinforcement layers augment shear stiffness and strength proportionally to the stiffness ratio, with negative Poisson's ratios enhancing lateral capacity while permitting stiffness tuning. Unitary stiffness ratio layers, though minimally invasive, yield marginal capacity gains. Cyclic analyses confirm auxetic reinforcements' superior strength augmentation, promoting elastic strain energy storage (ALLSE) while curtailing plastic dissipation (ALLPD) and damage dissipation (ALLDMD), contingent on layer stiffness.

The tunable macroscopic properties of metamaterials empower designers to achieve targeted strength enhancements while alleviating stiffness incompatibilities. Future industrial-scale production of auxetic metamaterials holds transformative potential for masonry retrofitting, facilitating optimal interventions as evidenced herein.

CRediT authorship contribution statement

Siro Casolo: Writing – review & editing, Supervision, Project administration, Methodology, Formal analysis, Conceptualization. **Giuseppina Uva:** Supervision, Resources, Methodology, Conceptualization. **Luis Carlos Martins da Silva:** Writing – original draft, Conceptualization. **Luigi Salvatore Rainone:** Writing – review & editing, Writing – original draft, Visualization, Methodology, Investigation, Formal analysis, Data curation.

Declaration of Competing Interest

The authors declare the following financial interests/personal relationships which may be considered as potential competing interests: Siro Casolo reports financial support was provided by Ministry of Education and Merit (PRIN2022_S). If there are other authors, they declare that they have no known competing financial interests or personal relationships that could have appeared to influence the work reported in this paper.

Acknowledgments

The authors Giuseppina Uva and Luigi S. Rainone acknowledges the financial support by FABRE - “Research consortium for the evaluation and monitoring of bridges, viaducts and other structures” (www.consorziofabre.it/en). The author Siro Casolo acknowledges the financial support of Ministero Italiano dell’Università e della Ricerca, "Bando relativo allo scorrimento delle graduatorie finali del bando PRIN 2022: Progetti di Ricerca di Rilevante Interesse Nazionale", Prot. 2022FLY8N7, Project title: “An integrated and fully discrete approach for the optimal topology design and the testing of meta-materials considering the non-linear geometric and elastic response”. Any opinion expressed in the paper does not necessarily reflect the view of the funder.

References

[1] P. Zampieri, N. Simoncello, C. Pellegrino, Seismic capacity of masonry arches with irregular abutments and arch thickness, Constr. Build. Mater. 201 (2019) 786–806, https://doi.org/10.1016/j.conbuildmat.2018.12.063.
[2] I. Puncello, S. Caprili, Seismic assessment of historical masonry buildings at different scale levels: a review, Appl. Sci. 13 (3) (2023) 1941, https://doi.org/10.3390/app13031941.
[3] L. Vargas, C. Sandoval, E. Bertolesi, S. Calderón, Seismic behavior of partially grouted masonry shear walls containing openings: experimental testing, Eng. Struct. 278 (2023) 115549, https://doi.org/10.1016/j.engstruct.2022.115549.
[4] S. Saari, B.A. Bakar, N.A. Surip, Correlation between compressive strength of interlocking compressed earth brick wall, prism, and single unit, Materials 8 (2025) 100643, https://doi.org/10.1016/j.nxmate.2025.100643.
[5] R. Maheshwari, Influence of bond pattern and brick type on the static compressive response of unreinforced brick masonry wallets, Materials 11 (2026) 101698, https://doi.org/10.1016/j.nxmate.2026.101698.
[6] S. Casolo, C.A. Sanjust, Seismic analysis and strengthening design of a masonry monument by a rigid body spring model: The “Maniace Castle” of Syracuse, Eng. Struct. 31 (7) (2009) 1447–1459, https://doi.org/10.1016/j.engstruct.2009.02.030.
[7] S. Bhattacharya, S. Nayak, S.C. Dutta, A critical review of retrofitting methods for unreinforced masonry structures, Int. J. Disaster Risk Reduct. 7 (2014) 51–67, https://doi.org/10.1016/j.ijdrr.2013.12.004.
[8] J. Thamboo, Performance of masonry columns confined with composites under axial compression: A stateof-the-art review, Constr. Build. Mater. 274 (2021) 121791, https://doi.org/10.1016/j.conbuildmat.2020.121791.
[9] K.S. Alotaibi, K. Galal, Experimental study of CFRP-confined reinforced concrete masonry columns tested under concentric and eccentric loading, Composites Part B Engineering 155 (2018) 257–271, https://doi.org/10.1016/j.compositesb.2018.08.024.
[10] M. Fossetti, G. Minafò, Comparative experimental analysis on the compressive behaviour of masonry columns strengthened by FRP, BFRCM or steel wires, Composites Part B Engineering 112 (2017) 112124, https://doi.org/10.1016/j.compositesb.2016.12.048.
[11] J. Wang, C. Wan, Q. Zeng, L. Shen, M.A. Malik, D. Yan, Effect of eccentricity on retrofitting efficiency of basalt textile reinforced concrete on partially damaged masonry columns, Compos. Struct. 232 (2020) 111585, https://doi.org/10.1016/j.compstruct.2019.111585.
[12] L.S. Rainone, L. Da Silva, G. Uva, S. Casolo, Dynamic behaviour of compressed masonry columns reinforced through innovative techniques. 10th ECCOMAS Thematic Conference on Computational Methods in Structural Dynamics and Earthquake Engineering, 2025, pp. 1–15, https://doi.org/10.7712/120125.12589.25177.
[13] X. Yu, J. Zhou, H. Liang, Z. Jiang, L. Wu, Mechanical metamaterials associated with stiffness, rigidity and compressibility: A brief review, Prog. Mater. Sci. 94 (2018) 114–173, https://doi.org/10.1016/j.pmatsci.2017.12.003.
[14] P. Jiao, J. Mueller, J.R. Raney, X. Zheng, A.H. Alavi, Mechanical metamaterials and beyond, Nat. Commun. 14 (1) (2023) 6004, https://doi.org/10.1038/s41467-023-41679-8.
[15] T.C. Lim, Metamaterial with tunable positive to negative Poisson’s ratio inspired by the Saint Andrew’s Cross, Materials 9 (2025) 100954, https://doi.org/10.1016/j.nxmate.2025.100954.

[16] M. Singh, A. Arjunan, A. Baroutaji, C.T. Wanniarachchi, A.S. Praveen, J. Robinson, A. Vance, M. Appiah, A. Arafat, Targeted mechanical and energy absorption properties of 3D printed aluminium metamaterials, Materials 7 (2025) 100356, https://doi.org/10.1016/j.nxmate.2024.100356.

[17] D. Edmund, M. Asad, C. Yan, T. Zahra, Experimental investigation on application of 3D-printed auxetic cementitious composites to strengthen concrete block masonry, ISSN 2352-0124, Structures 88 (2026) 111823, https://doi.org/10.1016/j.istruc.2026.111823.

[18] M. Hajsadeghi, L. Wan, E.O. Momoh, A. Jayasinghe, R. Vinai, P. Kripakaran, K. E. Evans, J.J. Orr, Compressive behaviour of mortar panels reinforced with polymeric auxetic lattices: Experimental testing and numerical modelling, ISSN 0950-0618, Constr. Build. Mater. 503 (2025) 144585, https://doi.org/10.1016/j.conbuildmat.2025.144585.

[19] Z. Meng, Y. Xu, W. Zhou, J. Xie, B. Šavija, Foamed cementitious composites with 3D-printed auxetic lattice reinforcement: enhancing static and cyclic performance, ISSN 1359-8368, Composites Part B Engineering 303 (2025) 112614, https://doi.org/10.1016/j.compositesb.2025.112614.

[20] S. Casolo, A linear-elastic heuristic-molecular modelling for plane isotropic micropolar and auxetic materials, Int. J. Solids Struct. 224 (2021) 111042, https://doi.org/10.1016/j.ijsolstr.2021.111042.

[21] L.C. da Silva, N. Grillanda, S. Casolo, Heuristic molecular modelling of quasi-isotropic auxetic metamaterials under large deformations, Int. J. Mech. Sci. 251 (2023) 108316, https://doi.org/10.1016/j.ijmecsci.2023.108316.

[22] L.C. da Silva, S. Casolo, Design of an auxetic and standard soft material for additive manufacturing using a heuristic RBSM approach, Eur. Congr. Comput. Methods Appl. Sci. Eng. (2024) 1–8, https://doi.org/10.23967/eccomas.2024.233.

[23] Dassault Systèmes Simulia Corp. ABAQUS/Standard User's Manual, Version 6.9, 2009.

[24] A. Borri, G. Castori, M. Corradi, Strengthening of fair face masonry columns with steel hooping, Mater. Struct. 47 (12) (2014) 2117–2130, https://doi.org/10.1617/s11527-014-0376-6.

[25] F. Micelli, M. Di Ludovico, A. Balsamo, G. Manfredi, Mechanical behaviour of FRP-confined masonry by testing of full-scale columns, Mater. Struct. 47 (12) (2014) 2081–2100, https://doi.org/10.1617/s11527-014-0357-9.

[26] M.A. Aiello, F. Micelli, L. Valente, FRP confinement of square masonry columns, J. Compo- sites Constr. 13 (2) (2009) 148–158, https://doi.org/10.1061/(ASCE)1090-0268(2009)13:2(148).

[27] M. Corradi, A. Grazini, A. Borri, Confinement of brick masonry columns with CFRP materials, Compos. Sci. Technol. 67 (9) (2007) 1772–1783, https://doi.org/10.1016/j.compscitech.2006.11.002.

[28] M. Di Ludovico, C. D'ambra, A. Prota, G. Manfredi, FRP confinement of tuff and clay brick columns: Experimental study and assessment of analytical models, J. Compos. Constr. 14 (5) (2010) 583–596, https://doi.org/10.1061/(ASCE)CC.1943-5614.000011.

[29] C. Faella, E. Martinelli, S. Paciello, G. Camorani, M.A. Aiello, F. Micelli, E. Nigro, Masonry columns confined by composite materials: Experimental investigation, Composites Part B Engineering 42 (4) (2011) 692–704, https://doi.org/10.1016/j.compositesb.2011.02.001.

[30] T.D. Krevaikas, T.C. Triantafillou, Masonry confinement with fiber-reinforced polymers, J. Compos. Constr. 9 (2) (2005) 128–135, https://doi.org/10.1061/(ASCE)10900268(2005)9:2(128).

[31] J. Lubliner, J. Oliver, S. Oller, E. Onate, A plastic-damage model for concrete, Int. J. Solids Struct. 25 (3) (1989) 299–326, https://doi.org/10.1016/0020-7683(89)90050-4.

[32] J. Lee, G.L. Fenves, Plastic-damage model for cyclic loading of concrete structures, J. Eng. Mech. 124 (8) (1998) 892–900, https://doi.org/10.1061/(ASCE)0733-9399(1998)124:8(892).

[33] L.S. Rainone, V. Tateo, S. Casolo, G. Uva, About the use of concrete damage plasticity for modeling masonry post-elastic behavior, Buildings 13 (8) (2023) 1915, https://doi.org/10.3390/buildings13081915.

[34] S. Dorji, H. Derakhshan, D.P. Thambiratnam, A. Mohyeddin, Lateral load response of semi-interlocking mortarless masonry-infilled frames, Structures 61 (2024) 105998, https://doi.org/10.1016/j.istruc.2024.105998.

[35] J.K. Bhaskar, D. Bhunia, L. Koutas, In-plane behaviour of masonry infill walls with openings strengthened using textile reinforced mortar, Structures 63 (2024) 106439, https://doi.org/10.1016/j.istruc.2024.106439.

[36] P. Pagni, G. Bartolini, A. De Falco, F. Landi, C. Resta, The Use of Concrete Damage Plasticity for Modeling Shear-Compression Tests on Stone Masonry Panels. International Conference Florence HeriTech: the Future of Heritage Science and Technologies, 2024, pp. 27–38, https://doi.org/10.1007/978-3-03198379-5_3.

[37] G. Duvaut, J.L. Lions, Les Inequations en Mecanique et en Physique, Dunod, Paris, 1972.